AGU PUBLICATIONS

JGR

Journal of Geophysical Research: Solid Earth

RESEARCH ARTICLE
10.1002/2015JB012702

Key Points:
- A new joint inversion algorithm of surface and body wave data is developed
- Surface wave dispersion data are also used to constrain V_p in the joint inversion
- New V_p and V_s models are developed for Southern California plate boundary region

Correspondence to:
H. Zhang,
zhang11@ustc.edu.cn

Citation:
Fang, H., H. Zhang, H. Yao, A. Allam, D. Zigone, Y. Ben-Zion, C. Thurber, and R. D. van der Hilst (2016), A new algorithm for three-dimensional joint inversion of body wave and surface wave data and its application to the Southern California plate boundary region, *J. Geophys. Res. Solid Earth*, *121*, 3557–3569, doi:10.1002/2015JB012702.

Received 1 DEC 2015
Accepted 18 APR 2016
Accepted article online 24 APR 2016
Published online 14 MAY 2016

A new algorithm for three-dimensional joint inversion of body wave and surface wave data and its application to the Southern California plate boundary region

Hongjian Fang[1], Haijiang Zhang[1], Huajian Yao[1], Amir Allam[2,3], Dimitri Zigone[2,4], Yehuda Ben-Zion[2], Clifford Thurber[5], and Robert D. van der Hilst[6]

[1]Laboratory of Seismology and Physics of Earth's Interior, School of Earth and Space Sciences, University of Science and Technology of China, Hefei, China, [2]Department of Earth Sciences, University of Southern California, Los Angeles, California, USA, [3]Now at Geophysical Institute and Department of Geology and Geophysics, University of Alaska Fairbanks, Fairbanks, Alaska, USA, [4]Now at Department of Meteorology and Geophysics, University of Vienna, Vienna, Austria, [5]Department of Geoscience, University of Wisconsin-Madison, Madison, Wisconsin, USA, [6]Department of Earth, Atmospheric, and Planetary Sciences, Massachusetts Institute of Technology, Cambridge, Massachusetts, USA

Abstract We introduce a new algorithm for joint inversion of body wave and surface wave data to get better 3-D *P* wave (V_p) and *S* wave (V_s) velocity models by taking advantage of the complementary strengths of each data set. Our joint inversion algorithm uses a one-step inversion of surface wave traveltime measurements at different periods for 3-D V_s and V_p models without constructing the intermediate phase or group velocity maps. This allows a more straightforward modeling of surface wave traveltime data with the body wave arrival times. We take into consideration the sensitivity of surface wave data with respect to V_p in addition to its large sensitivity to V_s, which means both models are constrained by two different data types. The method is applied to determine 3-D crustal V_p and V_s models using body wave and Rayleigh wave data in the Southern California plate boundary region, which has previously been studied with both double-difference tomography method using body wave arrival times and ambient noise tomography method with Rayleigh and Love wave group velocity dispersion measurements. Our approach creates self-consistent and unique models with no prominent gaps, with Rayleigh wave data resolving shallow and large-scale features and body wave data constraining relatively deeper structures where their ray coverage is good. The velocity model from the joint inversion is consistent with local geological structures and produces better fits to observed seismic waveforms than the current Southern California Earthquake Center (SCEC) model.

1. Introduction

Seismic tomography using body waves or surface waves has proven to be one of the most important and useful tools in investigating the structure of the Earth at local, regional, and global scales [e.g., *Simons et al.*, 1999; *Ritzwoller et al.*, 2001; *Zhang and Thurber*, 2003; *Li et al.*, 2008; *Lebedev and van der Hilst*, 2008; *Yao et al.*, 2010]. Ray-based traveltime tomography using body wave arrival times has been popular and effective because of its simplicity in theory and low computational requirements. However, it has drawbacks besides its high-frequency approximation. On the one hand, the shallow part of the model generally cannot be resolved well since there are not enough crossing rays. On the other hand, due to the limited quantity and lower quality of *S* wave observations caused by the contamination of the direct *S* wave arrival by *P* wave coda or other converted phases, the V_s model tends to have lower resolution and greater uncertainty than that of the V_p model. This makes the direct comparison between V_p and V_s models challenging.

Surface wave tomography based on ambient noise has been widely used to investigate regional crustal structure in the past decade [e.g., *Shapiro et al.*, 2005; *Sabra et al.*, 2005; *Yao et al.*, 2006; *Yang et al.*, 2007; *Lin et al.*, 2008] using a period band of 5–40 s. Moreover, recent studies show that shorter period (~1 s, using station spacing of ~20 km or less) surface waves can also be retrieved from ambient noise cross correlation [e.g., *Picozzi et al.*, 2009; *Huang et al.*, 2010; *Young et al.*, 2011; *Pilz et al.*, 2012; *Lin et al.*, 2013; *Shirzad and Shomali*, 2014]. Because the depth sensitivity depends on frequency, shorter period surface waves are more sensitive to the near-surface velocity and are thus particularly useful to resolve shallow V_s structure.

Separate inversions using body wave or surface wave data cannot provide a unified model that can fit both data sets, because of the resolution gap due to different data sensitivities. New inversion schemes that can fit both body wave and surface wave data have been proposed in order to take advantage of the complementary sensitivities of both data sets, allowing to produce more unified models of Earth structure. Such joint inversions have been done on a global scale [e.g., *Woodhouse and Dziewonski*, 1984; *Mégnin and Romanowicz*, 2000; *Antolik et al.*, 2003; *Lebedev and van der Hilst*, 2008], on a regional scale [e.g., *Friederich*, 2003; *West et al.*, 2004; *Obrebski et al.*, 2012; *Schmid et al.*, 2008; *Nunn et al.*, 2014a], and on a local scale [*Zhang et al.*, 2014; *Syracuse et al.*, 2015]. Alternatively, using the V_s model from surface wave tomography as a starting model can help improve the final results for teleseismic tomography [e.g., *Rawlinson and Fishwick*, 2012; *Nunn et al.*, 2014b]. Jointly inverting surface wave dispersion and body wave data has also been used in exploration geophysics to resolve laterally varying layered models better [*Boiero and Socco*, 2014].

In the joint inversion scheme of *Zhang et al.* [2014], surface wave dispersion measurements are only used to invert for V_s while V_p is obtained from inversion of body wave arrival times. In addition, the joint inversion scheme adopts the two-step approach in which phase or group velocity maps are first obtained from surface wave dispersion data and then a series of 1-D V_s profiles are solved at discrete grid nodes. Thus, the two-step strategy is not a straightforward way for a joint inversion of surface wave and body wave data to produce a 3-D model. Adjoint tomography can take advantage of the whole waveform information, but it is still computationally expensive [*Tape et al.*, 2009].

Here we propose a new joint inversion method to invert body wave arrival times and surface wave traveltime data, which avoids the above mentioned issues. Our joint inversion scheme combines pertinent aspects of the double-difference (DD) method of *Zhang and Thurber* [2003] for body wave arrival time inversion and the one-step surface wave inversion of *Fang et al.* [2015]. Compared to the joint inversion scheme of *Zhang et al.* [2014], the new method incorporates sensitivity of surface wave data with respect to V_p in addition to V_s. Therefore, the new method can improve the V_s model and shallow V_p model at the same time due to the fact that short-period Rayleigh wave measurements have relatively large sensitivity to V_p in the shallow crust [*Lin et al.*, 2014]. To show its utility, we apply the joint inversion method to body wave arrival time data from *Allam and Ben-Zion* [2012] and Rayleigh wave traveltime data obtained from ambient noise cross correlation from *Zigone et al.* [2015] in the Southern California plate boundary region.

2. Methodology

In this section, we first describe the inversions using only body wave arrival times or surface wave traveltime measurements and then followed by the joint inversion strategy using both data sets.

2.1. Body Wave Arrival Time Tomography

The body wave inversion is based on regional-scale double-difference (DD) tomography, which uses pseudobending ray tracing to calculate the traveltimes and raypaths between source-receiver pairs, and which inverts simultaneously for 3-D velocity variations and seismic event hypocenters using both absolute and differential arrival times [*Zhang and Thurber*, 2003]. The linearized DD tomography equation can be written in a matrix form [*Zhang and Thurber*, 2006] as

$$\begin{bmatrix} \mathbf{G}_H^{T_p} & \mathbf{G}_{V_p}^{T_p} & \mathbf{0} \\ \mathbf{G}_H^{T_s} & \mathbf{0} & \mathbf{G}_{V_s}^{T_s} \end{bmatrix} \begin{bmatrix} \mathbf{\Delta H} \\ \mathbf{\Delta m}_p \\ \mathbf{\Delta m}_s \end{bmatrix} = \begin{bmatrix} \mathbf{d}^{T_p} \\ \mathbf{d}^{Ts} \end{bmatrix}, \tag{1}$$

where $\mathbf{G}_H^{T_p}$, $\mathbf{G}_H^{T_s}$, $\mathbf{G}_{V_p}^{T_p}$, and $\mathbf{G}_{V_s}^{T_s}$ are the sensitivity matrices of first *P* and *S* arrival times with respect to hypocenter parameters, V_p and V_s, respectively; $\mathbf{\Delta H}$, $\mathbf{\Delta m}_p$, $\mathbf{\Delta m}_s$ are perturbations to hypocenter parameters, V_p, and V_s model parameters; and $\mathbf{d}^{T_p}$ and $\mathbf{d}^{T_s}$ are residuals for absolute or differential *P* and *S* arrival times.

2.2. One-Step Surface Wave Tomography

Fang et al. [2015] developed a one-step inversion method to invert surface wave dispersion measurements directly for 3-D variations in V_s without the intermediate step of constructing phase or group velocity maps in the inversion calculation. The fast marching method (FMM) [*Rawlinson and Sambridge*, 2004] is used to compute surface wave traveltimes and raypaths at each frequency, which avoids the assumption of great circle propagation. Ray tracing for surface waves has proven to be quite necessary, especially for short-period

dispersion data in areas with complex structure [*Fang et al.*, 2015]. The traveltime perturbation at each frequency ω with respect to a reference model for the path i is given by

$$\delta t_i(\omega) = t_i^{obs}(\omega) - t_i(\omega) \approx -\sum_{k=1}^{K} v_{ik} \frac{\delta C_k(\omega)}{C_k^2(\omega)}, \tag{2}$$

where $t_i^{obs}(\omega)$ is the observed surface wave traveltime, $t_i(\omega)$ is the calculated traveltime from a reference model that can be updated in the inversion, v_{ik} is the bilinear interpolation coefficients along the raypath associated with the ith traveltime data and the phase (or group) velocity $C_k(\omega)$ and its perturbation $\delta C_k(\omega)$ of the kth 2-D surface grid point at the frequency ω, respectively. Using 1-D depth kernels of Rayleigh wave phase or group velocity data to compressional velocity (V_p), shear velocity (V_s), and density (ρ) at each surface grid node, we can rewrite equation (2) as

$$\delta t_i(\omega) = \sum_{k=1}^{K} \left(-\frac{v_{ik}}{C_k^2} \right) \sum_{j=1}^{J} \left[\left. \frac{\partial C_k(\omega)}{\partial V_{pk}(z_j)} \right|_{\Theta_k} \delta V_{pk}(z_j) + \left. \frac{\partial C_k(\omega)}{\partial V_{sk}(z_j)} \right|_{\Theta_k} \delta V_{sk}(z_j) + \left. \frac{\partial C_k(\omega)}{\partial \rho_k(z_j)} \right|_{\Theta_k} \delta \rho_k(z_j) \right], \tag{3}$$

where Θ_k represents the 1-D reference model at the kth surface grid point on the surface and $V_{pk}(z_j)$, $V_{sk}(z_j)$ and $\rho_k(z_j)$ are the compression velocity, shear velocity, and mass density at the jth depth grid node, respectively. J is the number of grid points in the depth direction, and the number of total grid points of the 3-D model is $N = KJ$. The linearized equation of one-step surface wave inversion can be written as

$$\begin{bmatrix} \mathbf{G}_{V_p}^{SW} & \mathbf{G}_{V_s}^{SW} & \mathbf{G}_{\rho}^{SW} \end{bmatrix} \begin{bmatrix} \mathbf{\Delta m}_p \\ \mathbf{\Delta m}_s \\ \mathbf{\Delta \rho} \end{bmatrix} = \mathbf{d}^{SW}, \tag{4}$$

where $\mathbf{G}_{V_p}^{SW}$, $\mathbf{G}_{V_s}^{SW}$, and $\mathbf{G}_{\rho}^{SW}$ are sensitivity matrices of surface wave traveltime data with respect to V_p, V_s, and density, respectively; $\mathbf{\Delta m}_p$, $\mathbf{\Delta m}_s$, and $\mathbf{\Delta \rho}$ are perturbations to V_p, V_s, and density; and $\mathbf{d}^{SW}$ is the surface wave traveltime residuals at different frequencies. Following *Fang et al.* [2015], we used an empirical polynomial relationship between V_p and density [*Brocher*, 2005, equation (1)] to relate the sensitivity of surface wave data with respect to density to V_p. As a result, equation (4) can be rewritten as

$$\begin{bmatrix} \mathbf{G}_{V_p}^{SW} + R_\rho \mathbf{G}_{\rho}^{SW} & \mathbf{G}_{V_s}^{SW} \end{bmatrix} \begin{bmatrix} \mathbf{\Delta m}_p \\ \mathbf{\Delta m}_s \end{bmatrix} = \mathbf{d}^{SW}, \tag{5}$$

where $R_\rho = \sum_n n \chi_n V_p^{n-1}$ and χ_n represent the fitting polynomial coefficients between V_p and density. For simplicity, we did not consider the topography effect in surface wave inversion by assuming all stations to be on the average flat surface. But it should be possible to make an approximate correction for topography for surface waves by using a more sophisticated ray tracing approach that includes topography as a deformed "sheet."

2.3. Joint Inversion

With the above formulations it is straightforward to combine the surface wave data with the body wave data into a single framework. Specifically, we combine equations (1) and (5) into a single matrix for joint inversion as follows:

$$\begin{bmatrix} \mathbf{G}_H^{T_p} & \mathbf{G}_{V_p}^{T_p} & \mathbf{0} \\ \mathbf{G}_H^{T_s} & \mathbf{0} & \mathbf{G}_{V_s}^{T_s} \\ \mathbf{0} & \alpha \left(\mathbf{G}_{V_p}^{SW} + R_\rho \mathbf{G}_{\rho}^{SW} \right) & \alpha \mathbf{G}_{V_s}^{SW} \end{bmatrix} \begin{bmatrix} \mathbf{\Delta H} \\ \mathbf{\Delta m}_p \\ \mathbf{\Delta m}_s \end{bmatrix} = \begin{bmatrix} \mathbf{d}^{T_p} \\ \mathbf{d}^{Ts} \\ \alpha \mathbf{d}^{SW} \end{bmatrix}, \tag{6}$$

where α is the weight used to balance the two data types to prevent the results from being dominated by either one. Choosing an appropriate weight between the two data sets is nontrivial, however, due to the fact that they are sensitive to different parts of the model space and because the noise levels for different data types are different and in most cases unknown. This can be addressed by using the variances of the two data sets to normalize the objective function to avoid one data set controlling the joint inversion [*Julia et al.*, 2000; *Obrebski et al.*, 2012]. *Zhang et al.* [2014] used a trade-off analysis strategy to find an optimal weight value that corresponds to a model fitting both data sets equally well. However, this strategy is not efficient because of the

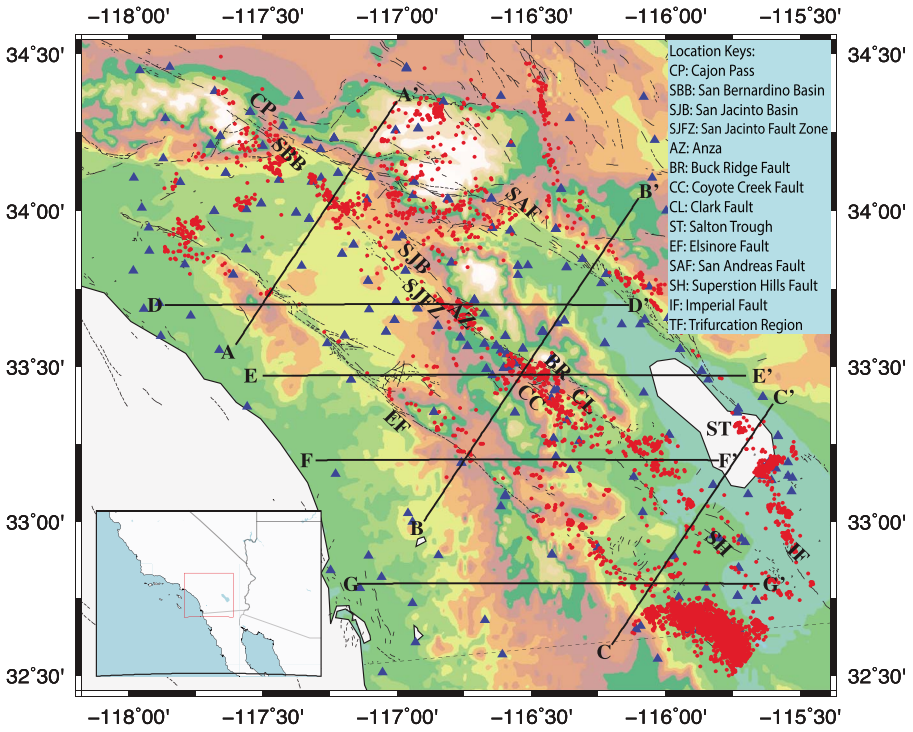

Figure 1. Map of the Southern California plate boundary region. The blue triangles and red dots show stations and earthquakes used in this study. Major faults are shown as fine black lines. Thick black lines depict the vertical profiles shown in Figures 4, 7, 10, and 11. The background colors indicate topography, with green and brown being low and high elevations, respectively. The inset indicates location of the study area in California.

large number of weights that need to be tested. In our case, it is easier to choose a reasonable weight because both data sets are in terms of time. For our joint inversion scheme we need to estimate the data variances of the two data sets and then normalize them.

Moreover, the joint inversion system in equation (6) is generally ill conditioned. Therefore, we adopted a smoothing regularization method to stabilize the inversion [*Aster et al.*, 2013]. In addition, because the V_p/V_s ratio model derived from the V_p and V_s models could vary greatly beyond the reasonable ranges, we also add

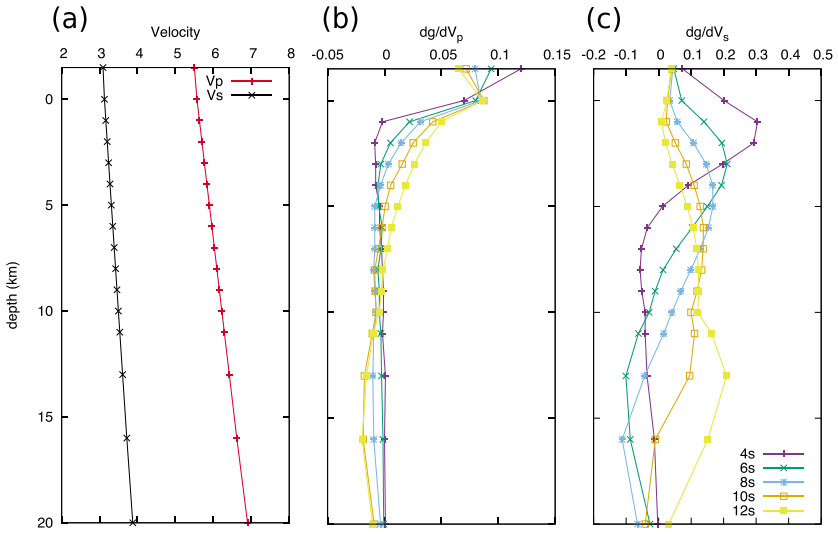

Figure 2. The (a) initial 1-D velocity model and the frequency-dependent sensitivity of Rayleigh wave group velocity to variations in (b) V_p and (c) V_s.

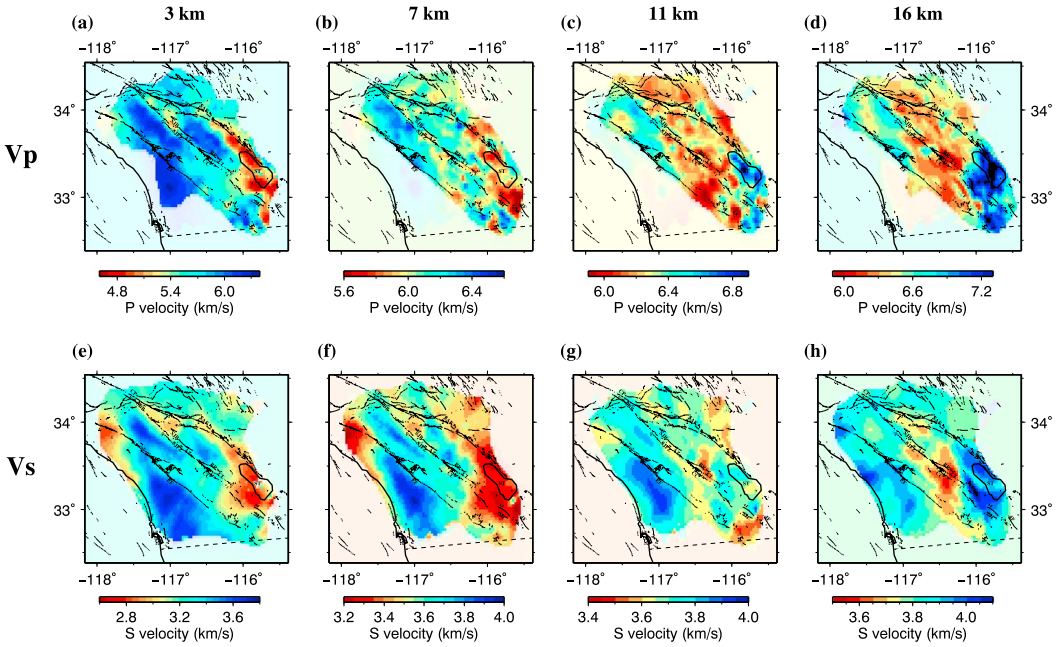

Figure 3. Horizontal slices of (a–d) V_p and (e–h) V_s at depths of 3 km, 7 km, 11 km, and 16 km from the joint inversion.

a constraint on the V_p/V_s ratio. The regularized inversion system is as follows:

$$\begin{bmatrix} \mathbf{G}_H^{T_p} & \mathbf{G}_{V_p}^{T_p} & \mathbf{0} \\ \mathbf{G}_H^{T_s} & \mathbf{0} & \mathbf{G}_{V_s}^{T_s} \\ \mathbf{0} & \alpha\left(\mathbf{G}_{V_p}^{SW} + R_\rho \mathbf{G}_\rho^{SW}\right) & \alpha\mathbf{G}_{V_s}^{SW} \\ \mathbf{0} & \beta_1\mathbf{L} & \mathbf{0} \\ \mathbf{0} & \mathbf{0} & \beta_2\mathbf{L} \\ \mathbf{0} & \beta_3\mathbf{I} & -\beta_3\eta\mathbf{I} \end{bmatrix} \begin{bmatrix} \Delta\mathbf{H} \\ \Delta\mathbf{m}_p \\ \Delta\mathbf{m}_s \end{bmatrix} = \begin{bmatrix} \mathbf{d}^{T_p} \\ \mathbf{d}^{T_s} \\ \alpha\mathbf{d}^{SW} \\ \mathbf{0} \\ \mathbf{0} \\ \beta_3\eta\mathbf{m}_s - \beta_3\mathbf{m}_p \end{bmatrix}, \tag{7}$$

where **L** is the model smoothing operator, and β_1, β_2, and β_3 are the weighting parameters balancing data fitting and model regularization terms, respectively. **L** is usually chosen as the first- or second-order spatial derivative operator. $\mathbf{m}_s$ and $\mathbf{m}_p$ are the V_s and V_p models from a previous iteration, and η is the reference V_p/V_s

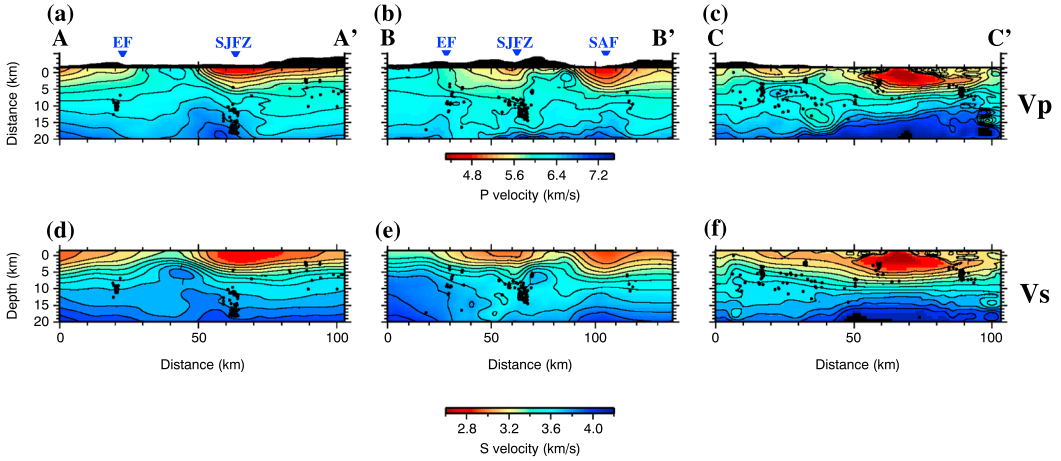

Figure 4. Fault-normal cross sections of (a–c) V_p and (d–f) V_s from the joint inversion along the lines of section AA′, BB′, and CC′, respectively. Relocated earthquakes are shown as black dots. The locations of the cross sections are plotted in Figure 1.

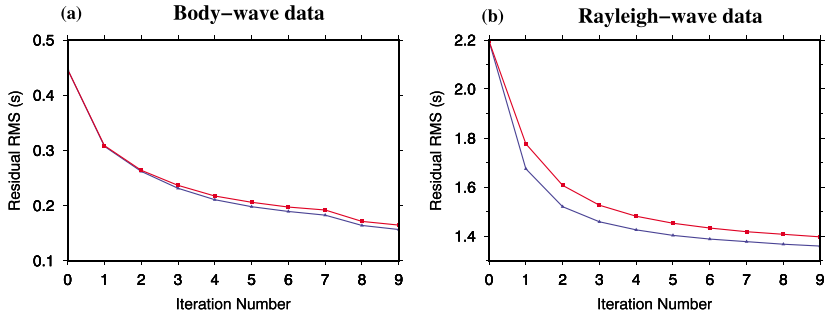

Figure 5. Reduction in the residuals for (a) the body wave arrival times and (b) the Rayleigh wave data along with iterations for joint inversion (red line) and separate Rayleigh wave only inversion (blue line).

ratio. Note that the last row in equation (7) is basically $(\mathbf{m}_p + \Delta\mathbf{m}_p) = \eta(\mathbf{m}_s + \Delta\mathbf{m}_s)$, which prevents V_p/V_s from becoming unrealistically small or large; η can be chosen based on a priori information about V_p/V_s in the study area. β_1, β_2, and β_3 can be chosen using the L-curve method [*Aster et al.*, 2013]. Equation (7) is solved for model perturbations $\mathbf{\Delta M}$ ($\mathbf{\Delta H}$, $\mathbf{\Delta m}_p$, $\mathbf{\Delta m}_s$) using the LSMR algorithm, which is based on Golub-Kahan bidiagonalization and can converge faster than the commonly used LSQR [*Fong and Saunders*, 2011]. Then the new reference model $\mathbf{M}_{i+1}$ for (i+1)th iteration can be obtained by

$$\mathbf{M}_{i+1} = \mathbf{M}_i + \Delta\mathbf{M}, \tag{8}$$

which is used for computing surface wave phase or group velocity maps and updating new raypaths for surface waves at each period. The body wave paths are also updated from the newly obtained velocity model. The process is repeated until further reduction of the residual variances for both data sets is insignificant.

3. Application to the Southern California Plate Boundary Region

We applied our joint inversion method to the Southern California plate boundary region using body wave data from *Allam and Ben-Zion* [2012] and Rayleigh wave data from *Zigone et al.* [2015] (Figure 1). The body wave data include 203,996 *P* and 45,511 *S* wave phase picks from 5493 events recorded at 139 stations, and 249,373 differential times computed from the phase picks. Figure 1 shows the distribution of stations and

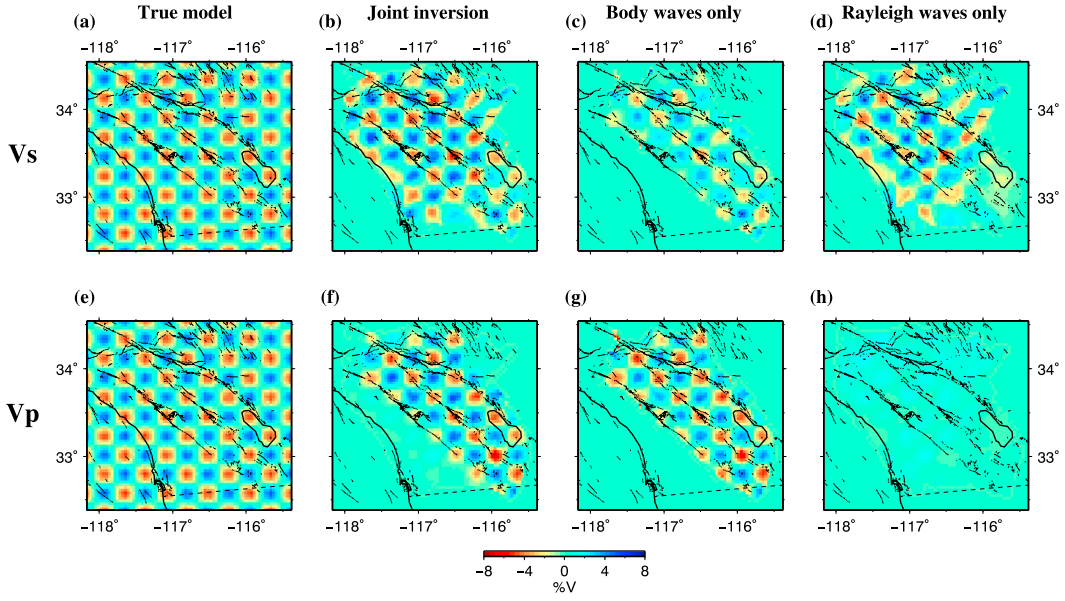

Figure 6. Comparison of recovered checkerboard models using body waves or Rayleigh waves at 7 km depth. (a) Input V_s model, (b) recovered V_s model from joint inversion of body and Rayleigh waves, (c) recovered V_s model using body waves only, and (d) recovered V_s model using Rayleigh waves only; (e) input V_p model, (f) recovered V_p model from joint inversion, (g) recovered V_p model using body waves only, and (h) recovered V_p model using Rayleigh waves only.

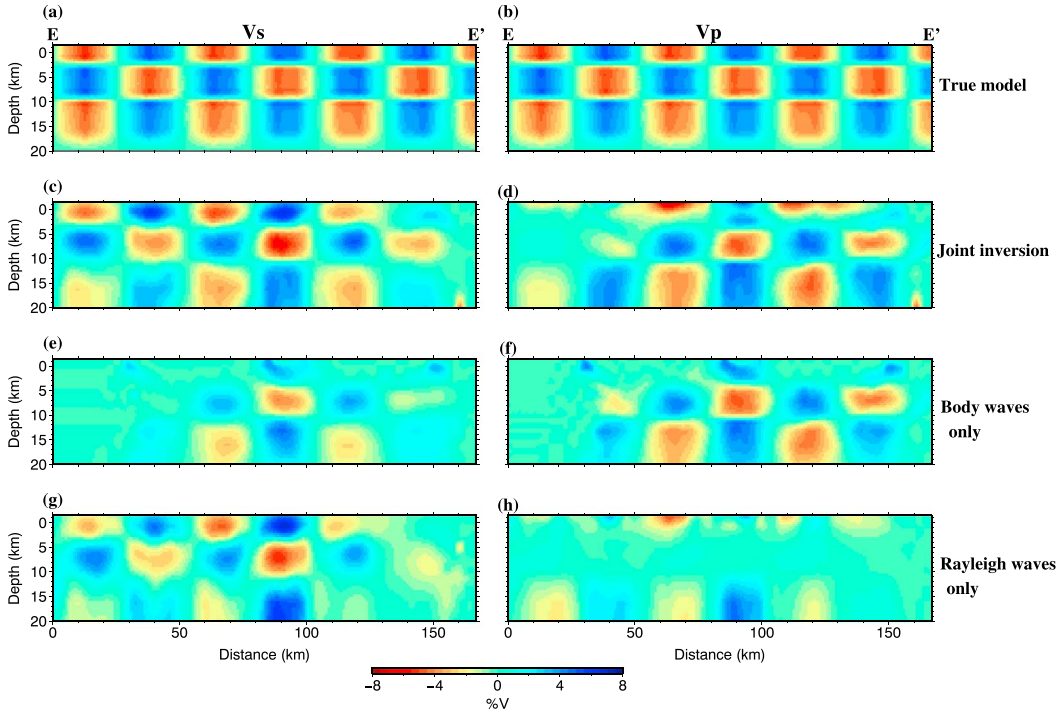

Figure 7. Comparison of recovered checkerboard models for (a, c, e, g) V_s and (b, d, f, h) V_p along section EE′ (for location see Figure 1). Figures 7a and 7b show the true models; Figures 7c and 7d show the recovered models from joint inversion; Figures 7e and 7f show the recovered models from body wave only inversion, and Figures 7g and 7h show the recovered models from Rayleigh wave only inversion, respectively.

earthquakes, as well as the topography and major faults in the study region. The Rayleigh wave data set includes 30,377 group traveltimes with periods ranging from 3 to 12 s between stations shown in Figure 1, which are extracted from ambient noise cross correlation using the modified preprocessing procedure of *Poli et al.* [2013]. Rayleigh waves within this period range are mostly sensitive to V_s, but at shallow depth the sensitivity to V_p is not insignificant (Figure 2). In the current joint inversion system, we do not consider azimuthal anisotropy, although it has been shown there exists strong azimuthal anisotropy in the study region [*Zigone et al.*, 2015]. Love wave group traveltimes are not included in the inversion since they are more sensitive to the azimuthal anisotropy than the Rayleigh wave. For the joint inversion, the study region is meshed with 94 by 73 grid nodes with an interval of 0.03° in both latitude and longitude, and the grid nodes in depth are positioned at −1.5, 0.0, 1.0, 2.0, 3.0, 4.0, 5.0, 6.0, 7.0, 8.0, 9.0, 10.0, 11.0, 13.0, 16.0, and 20.0 km, respectively. The initial model is the same as the simple 1-D velocity model used in *Allam and Ben-Zion* [2012]. We jointly solve for V_p, V_s, and earthquake hypocenters based on equation (7) and set η as 1.73 (that is, a Poisson solid). The weighting parameter α in equation (7) is chosen to be 0.3 based on

$$\alpha = \sqrt{\frac{N_p\sigma_p^2 + N_s\sigma_s^2}{N_{SW}\sigma_{SW}^2}} \tag{9}$$

following the strategy of *Julia et al.* [2000], where N_p, N_s, and N_{SW} are the number of *P* arrival times, *S* arrival times, and surface wave traveltimes, respectively; σ_p, σ_s, and σ_{SW} are the estimated uncertainty for each data set, respectively. In our case, the estimated uncertainty in body wave *P* arrival time is about 0.05 s, 0.11 s for *S* arrival time, and 1.3 s for surface wave data [*Allam and Ben-Zion*, 2012; *Zigone et al.*, 2015]. We chose the values of β_1 and β_2 as 100 and β_3 as 80 for the joint inversion system through a trade-off analysis.

Figure 3 shows the final V_p and V_s models at different depths, which are generally consistent with *Allam and Ben-Zion* [2012] and *Zigone et al.* [2015]. At shallow depths, we observe clear velocity contrasts across the major faults. Across the San Jacinto Fault Zone (SJFZ), in the depth slice of 3 km, both the V_p and V_s models show the right-lateral offset of two high-velocity bodies. The San Andreas Fault (SAF) is marked by slow seismic

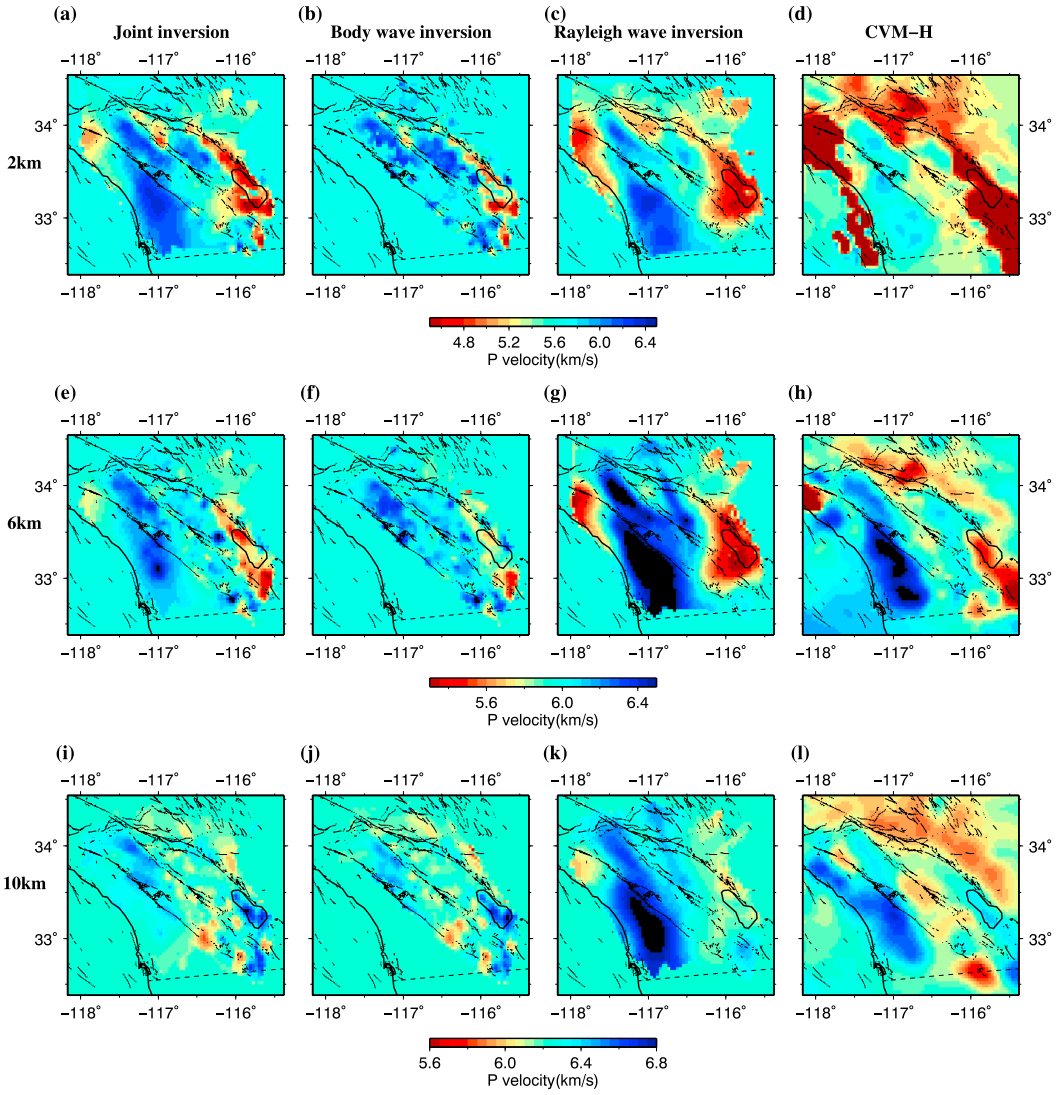

Figure 8. Horizontal slices of V_p at depths of 2, 6, and 10 km from (a, e, i) joint inversion, (b, f, j) separate inversion using body waves only, (c, g, k) separate inversion using Rayleigh waves only, and (d, h, l) from CVM-H [*Shaw et al.*, 2015].

wave propagation in the top 5 km, which is more evident in zones of structural complexity located to the eastern edge of the study region (Figures 3a, 3b, 3d, and 3e). The Salton Trough is associated with low-velocity anomalies at shallow depths <7 km but high-velocity anomalies at greater depths. Velocities are higher to the southeast of the Elsinore Fault (EF). Cross sections perpendicular to the fault strike reveal velocity contrasts across the EF, SJFZ, and SAF (Figure 4). The locations of relocated events are (within tens of meters) similar to those of *Allam and Ben-Zion* [2012]. These events are generally vertically distributed and associated with relatively high velocity zones.

4. Discussion

We have developed a joint inversion method to invert body wave and surface wave data simultaneously for 3-D V_p and V_s models. As expected, the V_p and V_s models produced by the joint inversion do not fit the individual data set as well as the models produced by separate inversions of body wave and surface wave data, but the differences are small (Figure 5).

Checkerboard resolution tests are used to investigate the performance of our algorithm (relative to separate inversions of the data sets) and provide a qualitative assessment of model resolution. We first construct a checkerboard model with alternating high- and low-velocity anomalies with horizontal dimensions of about

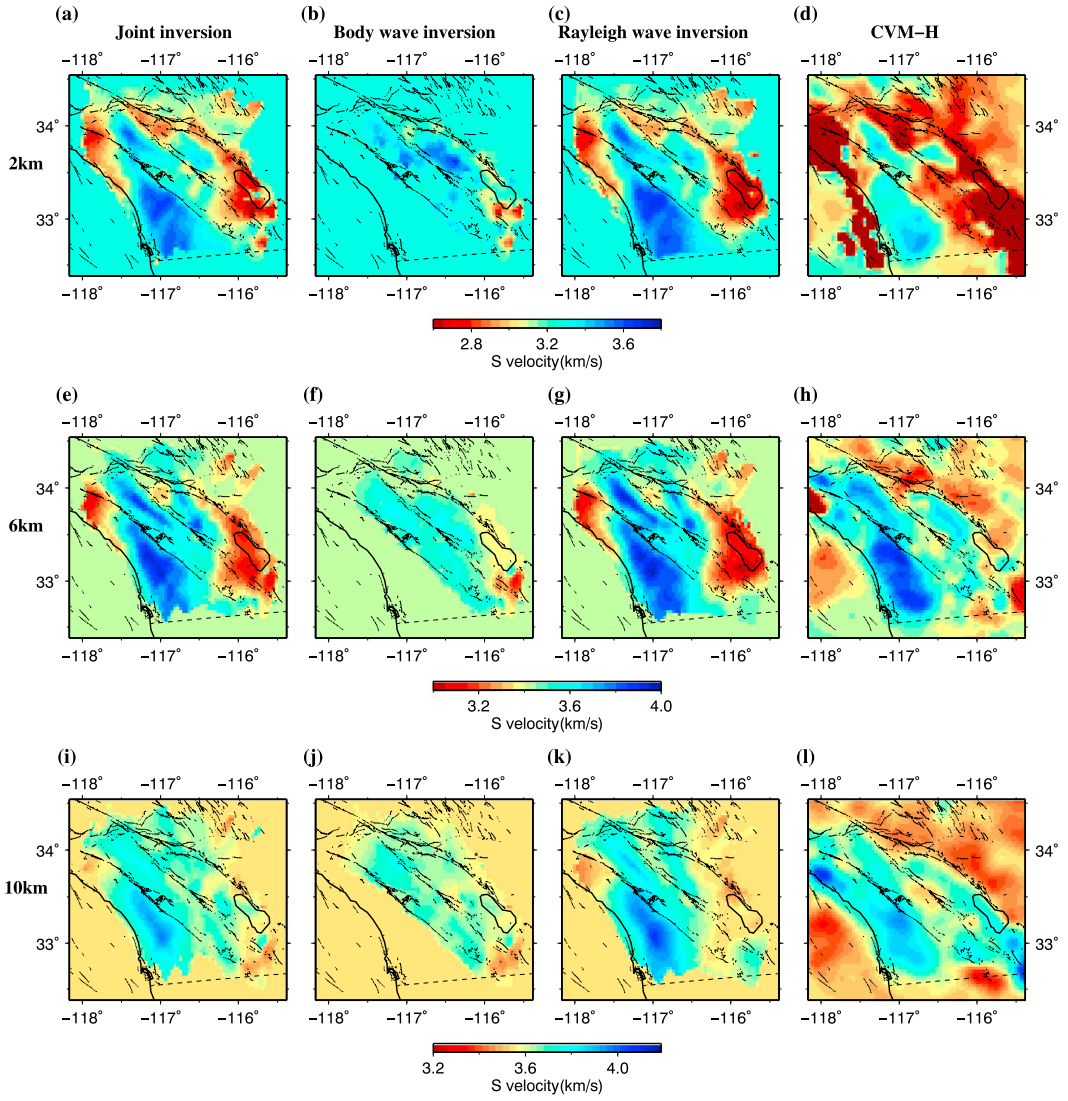

Figure 9. Horizontal slices of V_s at depths of 2, 6, and 10 km from (a, e, i) joint inversion, (b, f, j) separate inversion using body waves only, (c, g, k) separate inversion using Rayleigh waves only, and (d, h, l) from CVM-H [*Shaw et al.*, 2015].

25 by 25 km. Then we calculate body wave traveltimes and raypaths by the pseudobending ray tracing method and compute the traveltimes for Rayleigh waves with FMM using the 2-D group velocity maps at each period. Uniformly distributed random noise is added to *P* wave arrival times within the range of 0.05 s, to *S* wave arrival times within the range of 0.11 s, and to the surface wave traveltimes within the range of 1.3 s. The same inversion strategy is applied to the synthetic data to recover the checkerboard models. Figures 6 and 7 show comparisons of recovered checkerboard patterns for V_p and V_s models at the depth slice of 7 km and in cross section D-D′ using only body wave arrival times, only Rayleigh wave data, and both data sets. This comparison shows that the incorporation of Rayleigh wave data greatly improves V_s model resolution compared to the case of using only body wave data. At 7 km depth (Figure 6), the V_s model is poorly resolved by *S* wave arrival times. This is also the case at shallow depths due to sparse ray coverage (Figure 7). By using both body wave and Rayleigh wave data, the V_s model is better resolved from shallow to deep regions. The resolution for the V_p model at shallow depths is somewhat better in the joint inversion than the separate body wave inversion (Figure 7). This is because the short-period surface wave data also has some sensitivity to V_p (Figure 2). At depth larger than 5 km the V_p model is mainly resolved by *P* wave arrival times, thus the V_p model resolutions

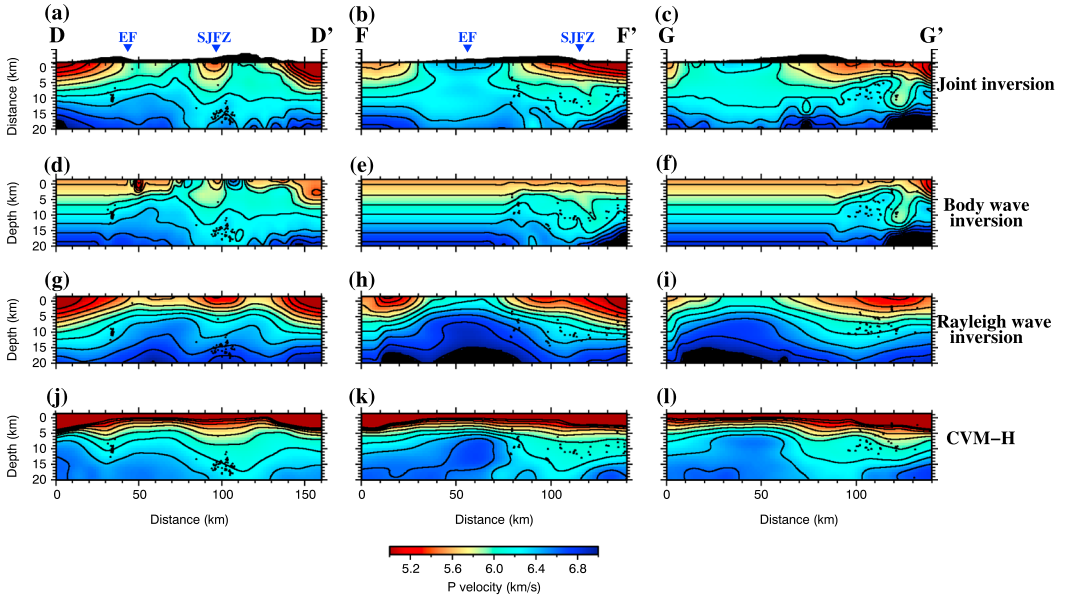

Figure 10. Vertical slices of V_p through cross sections DD′, FF′, and GG′ from (a–c) joint inversion, (d–f) separate inversion using body waves only, (g–i) separate inversion using Rayleigh waves only, and (j–l) from CVM-H [*Shaw et al.*, 2015]. The locations of the cross sections are plotted in Figure 1.

in this region are comparable to separate inversion using only body wave arrival times. For the V_s model, even if it is well resolved by Rayleigh wave traveltimes alone, the inclusion of body wave arrival times does improve its resolution, especially at depths greater than 7 km (Figures 6 and 7).

Figures 8 and 9 compare the horizontal slices of V_p and V_s models at different depths from separate and joint inversions. For the region between the shoreline and the EF, the resolution of V_p variations from the body wave only inversion is because there are very few earthquakes there. In comparison, the corresponding resolution of V_p variations in the joint inversion increases due to the availability of the Rayleigh wave data and its sensitivity to V_p at shallow depths. The high V_p anomaly revealed by the joint inversion for the region between the

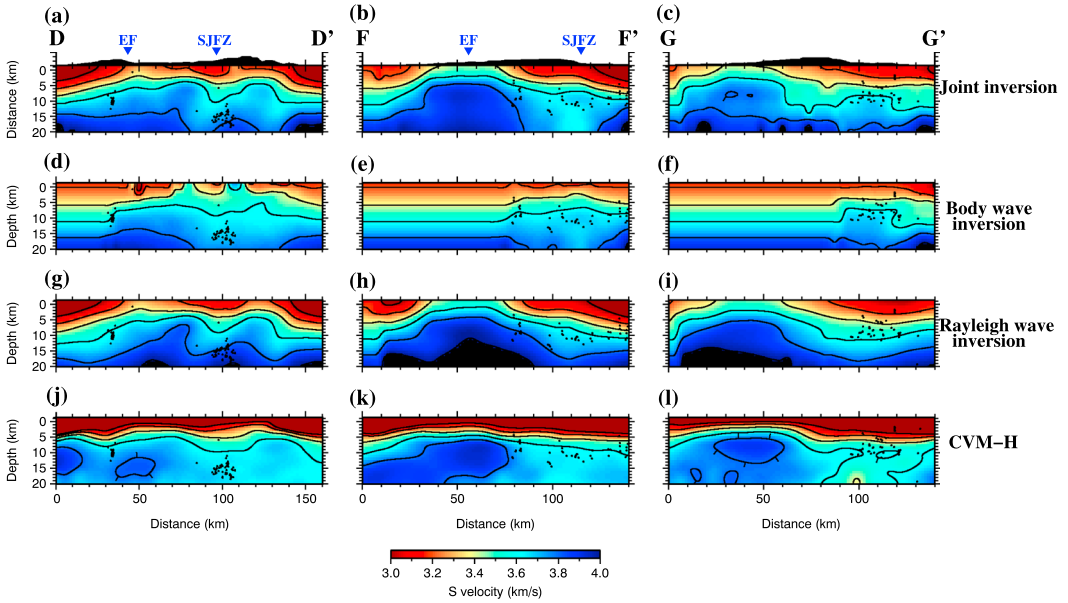

Figure 11. Vertical slices of V_s along cross sections DD′, FF′, and GG′ from (a–c) joint inversion, (d–f) separate inversion using body waves only, (g–i) separate inversion using Rayleigh waves only, and (j–l) from CVM-H [*Shaw et al.*, 2015]. The locations of the cross sections are plotted in Figure 1.

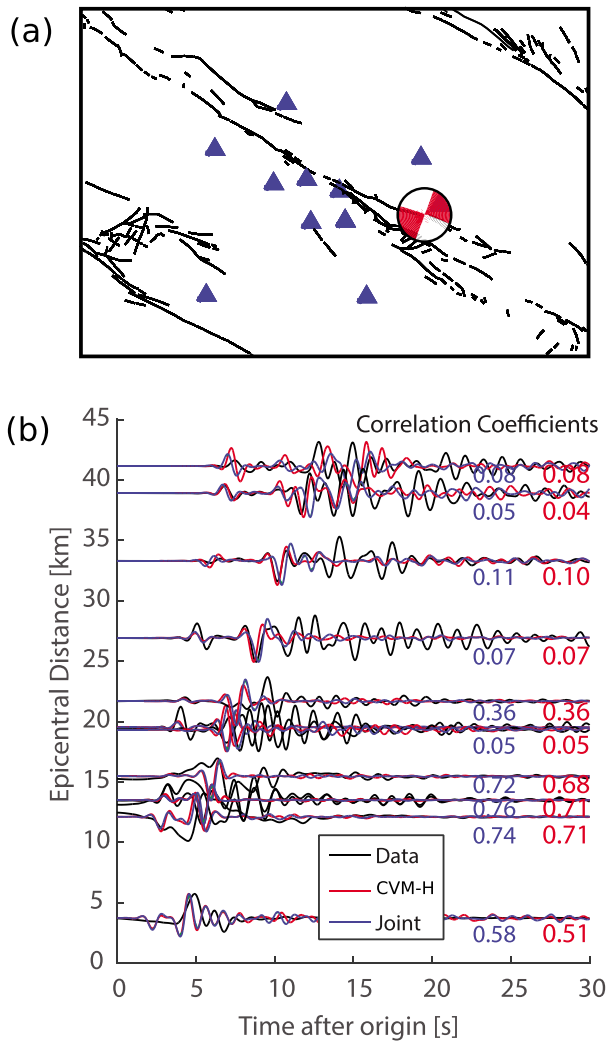

Figure 12. (a) Source and receiver geometry used for waveform simulations using the velocity model from our joint inversion. (b) Comparison of vertical velocity data (black) with waveform simulations using the jointly inverted model (blue) and the CVM-H (red) computed in SPECFEM3D. The records are low pass filtered with corner frequency 1 Hz. The correlation coefficient between the synthetic and data waveforms is shown for each model and source-receiver combination. The jointly inverted model modestly but consistently outperforms CVM-H in terms of both phase and amplitude, as shown by the slightly higher correlation coefficients.

shoreline and EF corresponds to the Peninsular Ranges batholith [*Barak et al.*, 2015]. The resolution of V_s variations from the joint inversion is high, which is to be expected because both the body wave and surface wave data have significant sensitivity to V_s. For example, at 2 km depth, the low V_s features at the intersection of the SJF and SAF as well as around the Salton Trough are more evident from the joint inversion than body wave only inversion (Figure 9). Along the SAF, the low V_s anomaly associated with the fault zone is more concentrated around the Salton Trough by the joint inversion than the surface wave only inversion. Compared to the Southern California Earthquake Center (SCEC) Community Velocity Model-Harvard (CVM-H 15.1.0, hereafter called CVM-H), which includes full 3-D waveform tomographic results [*Shaw et al.*, 2015], our joint inversion model generally shows similar but sharper features (Figures 8 and 9). Figures 10 and 11 show cross sections of V_p and V_s models inverted from separate and joint inversions.

In general, our joint inversion V_p and V_s models show clear velocity contrasts across various faults. At 2 km depth, the inversion results reveal two high-velocity anomalies with similar size that are shifted horizontally along the SJF. The Salton Trough is associated with a low-velocity anomaly above 7 km and a high-velocity anomaly below 10 km, which can be explained by crustal thinning [*Fuis et al.*, 1984; *Lachenbruch et al.*, 1985].

In the cross sections, the earthquakes associated with the EF and SJFZ are generally vertically distributed (Figure 4), indicating the two faults dip vertically.

Both the checkerboard tests and the real data applications show that incorporation of Rayleigh waves can improve the V_p model at shallow depths, in spite of its small sensitivity. Compared to the V_p model from body wave only inversion, joint inversion incorporating surface wave data improves the V_s model because of the larger sensitivity of the data to V_s. For the Southern California plate boundary region, our final shear velocity model from the joint inversion is dominated by surface wave data at shallow depths (<5 km), while it is mostly controlled by body wave data at greater depths.

As a validation test, we simulate the seismic wavefield for a *M*4.7 earthquake (11 March 2013) using the spectral element method [*Komatitsch and Tromp*, 1999]. We perform two separate simulations, producing synthetic velocity seismograms for the jointly inverted model presented and for the CVM-H [*Shaw et al.*, 2015]. The employed discretization provides numerical accuracy up to 5 Hz. For both models, we quantify the misfit by measuring the cross-correlation delay times and correlation coefficient of the synthetic seismograms compared to the recorded data. Figure 12 shows a comparison of three different waveforms: the data, synthetic waveforms produced by the joint inversion model, and those produced by the CVM-H. For all stations considered, the joint inversion model modestly but consistently outperforms the CVM-H in terms of matching the recorded data. Both models generally fit the recorded *P* and *S* waves well but fail to match late-arriving high-amplitude phases at more distant stations.

5. Conclusions

We present a new joint inversion method for simultaneous inversion of body wave and surface wave data for 3-D variations in V_p and V_s. Our joint inversion scheme, which combines concepts from the DD tomography of *Zhang and Thurber* [2003] and the one-step surface wave inversion method of *Fang et al.* [2015], makes it straightforward to combine body wave arrival times and surface wave data into a single inversion system. A weighting scheme taking into account the quality and quantity of the two data types is used to balance the fitting of the respective data sets. Compared to the body wave only inversion, the synthetic checkerboard test shows that the joint inversion resolves the V_s model better because of the incorporation of Rayleigh wave data. Furthermore, the very shallow V_p structure can also be improved due to the sizable sensitivity to compressional velocity of the short-period surface wave data. As a proof of concept, we applied our method to the Southern California plate boundary region to obtain internally consistent 3-D models of V_p and V_s. The joint inversion results show that both the V_p and the V_s variations are better constrained than by separate inversions of body wave arrival time data or Rayleigh wave data. The validation with wavefield simulation shows that the jointly inverted model modestly but consistently outperforms CVM-H in terms of both phase and amplitude. Our jointly inverted model improves the ability of simulating earthquake waveforms and is helpful for a better understanding of the regional geology and could serve as a more appropriate starting model for full waveform tomography.

Acknowledgments
This research is supported by the Natural Science Foundation of China (41474039 and 41222028), the Fundamental Research Funds for the Central Universities (WK2080000053), and by the U.S. Department of Energy (DE-NA0001523). It is also supported by the Southern California Earthquake Center awards #15112 and #16226 (contribution 6199). SCEC is funded by NSF Cooperative Agreement EAR-1033462 and USGS Cooperative Agreement G12AC20038. The body wave arrival time data and Rayleigh wave dispersion data used in this study are from *Allam and Ben-Zion* [2012] and *Zigone et al.* [2015], and they are available upon request. We are grateful to the Associate Editor, Carl Tape, and an anonymous reviewer for their constructive comments, which are helpful for improving this paper. All the figures are created using GMT plotting software [*Wessel and Smith*, 1998].

References

Allam, A., and Y. Ben-Zion (2012), Seismic velocity structures in the Southern California plate-boundary environment from double-difference tomography, *Geophys. J. Int.*, *190*(2), 1181–1196.
Antolik, M., Y. J. Gu, G. Ekström, and A. M. Dziewonski (2003), J362D28: A new joint model of compressional and shear velocity in the Earth's mantle, *Geophys. J. Int.*, *153*(2), 443–466.
Aster, R. C., B. Borchers, and C. H. Thurber (2013), *Parameter Estimation and Inverse Problems*, Academic Press., Boston, Mass.
Barak, S., S. L. Klemperer, and J. F. Lawrence (2015), San Andreas Fault dip, Peninsular Ranges mafic lower crust and partial melt in the Salton Trough, Southern California, from ambient-noise tomography, *Geochem. Geophys. Geosyst.*, *16*, 3946–3972, doi:10.1002/2015GC005970.
Boiero, D., and L. V Socco (2014), Joint inversion of Rayleigh-wave dispersion and *P*-wave refraction data for laterally varying layered models, *Geophysics*, *79*(4), EN49–EN59.
Brocher, T. M. (2005), Empirical relations between elastic wavespeeds and density in the Earth's crust, *Bull. Seismol. Soc. Am.*, *95*(6), 2081–2092.
Fang, H., H. Yao, H. Zhang, Y.-C. Huang, and R. D. van der Hilst (2015), Direct inversion of surface wave dispersion for three-dimensional shallow crustal structure based on ray tracing: Methodology and application, *Geophys. J. Int.*, *201*(3), 1251–1263.
Fong, D. C.-L., and M. Saunders (2011), LSMR: An iterative algorithm for sparse least-squares problems, *SIAM J. Sci. Comput.*, *33*(5), 2950–2971.
Friederich, W. (2003), The S-velocity structure of the East Asian mantle from inversion of shear and surface waveforms, *Geophys. J. Int.*, *153*(1), 88–102.
Fuis, G., W. Mooney, J. Healy, G. McMechan, and W. Lutter (1984), A seismic refraction survey of the Imperial Valley region, California, *J. Geophys. Res.*, *89*(B2), 1165–1189.
Huang, Y.-C., H. Yao, B.-S. Huang, R. D. van der Hilst, K.-L. Wen, W.-G. Huang, and C.-H. Chen (2010), Phase velocity variation at periods of 0.5–3 seconds in the Taipei Basin of Taiwan from correlation of ambient seismic noise, *Bull. Seismol. Soc. Am.*, *100*(5A), 2250–2263.

Julia, J., C. Ammon, R. Herrmann, and A. M. Correig (2000), Joint inversion of receiver function and surface wave dispersion observations, *Geophys. J. Int.*, *143*(1), 99–112.
Komatitsch, D., and J. Tromp (1999), Introduction to the spectral element method for three-dimensional seismic wave propagation, *Geophys. J. Int.*, *139*(3), 806–822.
Lachenbruch, A. H., J. Sass, and S. Galanis (1985), Heat flow in southernmost California and the origin of the Salton Trough, *J. Geophys. Res.*, *90*(B8), 6709–6736.
Lebedev, S., and R. D. van der Hilst (2008), Global upper-mantle tomography with the automated multimode inversion of surface and *S*-wave forms, *Geophys. J. Int.*, *173*(2), 505–518.
Li, C., R. D. van der Hilst, E. R. Engdahl, and S. Burdick (2008), A new global model for *P* wave speed variations in Earth's mantle, *Geochem. Geophys. Geosyst.*, *9*, Q05018.
Lin, F.-C., M. P. Moschetti, and M. H. Ritzwoller (2008), Surface wave tomography of the western United States from ambient seismic noise: Rayleigh and Love wave phase velocity maps, *Geophys. J. Int.*, *173*(1), 281–298.
Lin, F.-C., D. Li, R. W. Clayton, and D. Hollis (2013), High-resolution 3D shallow crustal structure in Long Beach, California: Application of ambient noise tomography on a dense seismic array, *Geophysics*, *78*(4), Q45—Q56.
Lin, F.-C., V. C. Tsai, and B. Schmandt (2014), 3-D crustal structure of the western United States: Application of Rayleigh-wave ellipticity extracted from noise cross-correlations, *Geophys. J. Int.*, *198*, 656–670.
Mégnin, C., and B. Romanowicz (2000), The three-dimensional shear velocity structure of the mantle from the inversion of body, surface and higher-mode waveforms, *Geophys. J. Int.*, *143*(3), 709–728.
Nunn, C., S. W. Roecker, K. F. Priestley, X. Liang, and A. Gilligan (2014a), Joint inversion of surface waves and teleseismic body waves across the Tibetan collision zone: The fate of subducted Indian lithosphere, *Geophys. J. Int.*, *198*(3), 1526–1542.
Nunn, C., et al. (2014b), Imaging the lithosphere beneath NE Tibet: Teleseismic *P* and *S* body wave tomography incorporating surface wave starting models, *Geophys. J. Int.*, *196*(3), 1724–1741.
Obrebski, M., R. M. Allen, F. Zhang, J. Pan, Q. Wu, and S.-H. Hung (2012), Shear wave tomography of China using joint inversion of body and surface wave constraints, *J. Geophys. Res.*, *117*, B01311, doi:10.1029/2011JB008349.
Picozzi, M., S. Parolai, D. Bindi, and A. Strollo (2009), Characterization of shallow geology by high-frequency seismic noise tomography, *Geophys. J. Int.*, *176*(1), 164–174.
Pilz, M., S. Parolai, M. Picozzi, and D. Bindi (2012), Three-dimensional shear wave velocity imaging by ambient seismic noise tomography, *Geophys. J. Int.*, *189*(1), 501–512.
Poli, P., H. Pedersen, M. Campillo, and the POLENET/LAPNET Working Group (2013), Noise directivity and group velocity tomography in a region with small velocity contrasts: The northern Baltic shield, *Geophys. J. Int.*, *192*(1), 413–424.
Rawlinson, N., and S. Fishwick (2012), Seismic structure of the southeast Australian lithosphere from surface and body wave tomography, *Tectonophysics*, *572*, 111–122.
Rawlinson, N., and M. Sambridge (2004), Wavefront evolution in strongly heterogeneous layered media using the fast marching method, *Geophys. J. Int.*, *156*(3), 631–647.
Ritzwoller, M. H., N. M. Shapiro, A. L. Levshin, and G. M. Leahy (2001), Crustal and upper mantle structure beneath Antarctica and surrounding oceans, *J. Geophys. Res.*, *106*(B12), 30,645–30,670.
Sabra, K. G., P. Gerstoft, P. Roux, W. Kuperman, and M. C. Fehler (2005), Surface wave tomography from microseisms in Southern California, *Geophys. Res. Lett.*, *32*, L14311, doi:10.1029/2005GL023155.
Schmid, C., S. Van der Lee, J. C. Vandecar, E. R. Engdahl, and D. Giardini (2008), Three-dimensional S velocity of the mantle in the Africa-Eurasia plate boundary region from phase arrival times and regional waveforms, *J. Geophys. Res.*, *113*, B03306, doi:10.1029/2005JB004193.
Shapiro, N. M., M. Campillo, L. Stehly, and M. H. Ritzwoller (2005), High-resolution surface-wave tomography from ambient seismic noise, *Science*, *307*(5715), 1615–1618.
Shaw, J. H., et al. (2015), Unified structural representation of the Southern California crust and upper mantle, *Earth Planet. Sci. Lett.*, *415*, 1–15.
Shirzad, T., and Z. H. Shomali (2014), Shallow crustal structures of the Tehran basin in Iran resolved by ambient noise tomography, *Geophys. J. Int.*, *196*(2), 1162–1176.
Simons, F. J., A. Zielhuis, and R. D. van der Hilst (1999), The deep structure of the Australian continent from surface wave tomography, *Dev. Geotectonics*, *24*, 17–43.
Syracuse, E., M. Maceira, H. Zhang, and C. Thurber (2015), Seismicity and structure of Akutan and Makushin Volcanoes, Alaska, using joint body and surface wave tomography, *J. Geophys. Res. Solid Earth*, *120*(2), 1036–1052.
Tape, C., Q. Liu, A. Maggi, and J. Tromp (2009), Adjoint tomography of the Southern California crust, *Science*, *325*(5943), 988–992.
Wessel, P., and W. H. Smith (1998), New, improved version of Generic Mapping Tools released, *Eos, Trans. AGU*, *79*(47), 579–579.
West, M., W. Gao, and S. Grand (2004), A simple approach to the joint inversion of seismic body and surface waves applied to the southwest US, *Geophys. Res. Lett.*, *31*, L15615, doi:10.1029/2004GL020373.
Woodhouse, J. H., and A. M. Dziewonski (1984), Mapping the upper mantle: Three-dimensional modeling of Earth structure by inversion of seismic waveforms, *J. Geophys. Res.*, *89*(B7), 5953–5986.
Yang, Y., M. H. Ritzwoller, A. L. Levshin, and N. M. Shapiro (2007), Ambient noise Rayleigh wave tomography across Europe, *Geophys. J. Int.*, *168*(1), 259–274.
Yao, H., R. D. van Der Hilst, and V. Maarten (2006), Surface-wave array tomography in SE Tibet from ambient seismic noise and two-station analysis I. Phase velocity maps, *Geophys. J. Int.*, *166*(2), 732–744.
Yao, H., R. D. van der Hilst, and J.-P. Montagner (2010), Heterogeneity and anisotropy of the lithosphere of SE Tibet from surface wave array tomography, *J. Geophys. Res.*, *115*(B12307), doi:10.1029/2009JB007142.
Young, M., N. Rawlinson, P. Arroucau, A. Reading, and H. Tkalčić (2011), High-frequency ambient noise tomography of southeast Australia: New constraints on Tasmania's tectonic past, *Geophys. Res. Lett.*, *38*, L13313, doi:10.1029/2011GL047971.
Zhang, H., and C. Thurber (2006), Development and applications of double-difference seismic tomography, *Pure Appl. Geophys.*, *163*(2–3), 373–403.
Zhang, H., and C. H. Thurber (2003), Double-difference tomography: The method and its application to the Hayward Fault, California, *Bull. Seismol. Soc. Am.*, *93*(5), 1875–1889.
Zhang, H., M. Maceira, P. Roux, and C. Thurber (2014), Joint inversion of body-wave arrival times and surface-wave dispersion for three-dimensional seismic structure around SAFOD, *Pure Appl. Geophys.*, *171*, 3013–3022.
Zigone, D., Y. Ben-Zion, M. Campillo, and P. Roux (2015), Seismic tomography of the Southern California plate boundary region from noise-based Rayleigh and Love waves, *Pure Appl. Geophys.*, *172*(5), 1007–1032.